

Compressive plasticity and toughness of a Ti-based bulk metallic glass

X.J. Gu^{a,*}, S.J. Poon^b, G.J. Shiflet^c, J.J. Lewandowski^a

^a Department of Materials Science and Engineering, Case Western Reserve University, Cleveland, OH 44106-7204, USA

^b Department of Physics, University of Virginia, Charlottesville, VA 22904-4714, USA

^c Department of Materials Science and Engineering, University of Virginia, Charlottesville, VA 22904-4745, USA

Received 8 September 2009; received in revised form 4 November 2009; accepted 10 November 2009

Abstract

The effects of changes in sample dimensions on the compressive plasticity and fracture toughness/energy have been determined for $\text{Ti}_{40}\text{Zr}_{25}\text{Cu}_{12}\text{Ni}_3\text{Be}_{20}$ bulk metallic glass (BMG). Changes in sample dimensions alone produced widely different values for compressive plasticity. While these were correlated with changes to the measured Poisson's ratio for samples of the same composition cast into different sample sizes, significant effects of testing conditions apart from the Poisson's ratio on the measured compressive plasticity are also demonstrated. Fracture toughness testing on the same material/size that exhibited zero compressive plasticity produced both notch and fatigue pre-cracked toughness in excess of $100 \text{ MPa m}^{1/2}$, while a size effect on the magnitude of toughness was similarly demonstrated. Discussions on the source(s) of the size effect on toughness are provided in addition to demonstrating that exceptional toughness can be obtained in this BMG which exhibits essentially zero compressive plasticity under certain test conditions. The apparent critical Poisson's ratio for plasticity/toughness is thus different in these very different types of tests.

© 2009 Acta Materialia Inc. Published by Elsevier Ltd. All rights reserved.

Keywords: Metallic glasses; Titanium alloys; Compressive plasticity; Toughness

1. Introduction

The attractive properties of bulk metallic glasses (BMGs), e.g. high strength and hardness, large elastic strain limits and in some systems, excellent corrosion- and wear resistance make them potentially useful for a variety of structural and functional applications [1–4]. However, BMGs can also exhibit less desirable properties such as low ductility/toughness and poor fatigue resistance at room temperature, which have severely limited their use as engineering materials. After decades of extensive research, synthesis of BMGs in some systems is now possible in sections up to several centimeters in diameter [5–14]. While making large size BMGs is no longer a central challenge, improving the damage tolerance (e.g., plasticity, toughness, and fatigue resistance) of BMGs has become one of the most important issues in the BMG community [3]. The detailed plastic deformation

mechanisms in metallic glasses are beginning to be modeled at different length scales. Inhomogeneous plastic deformation of BMGs is proposed to occur by initiation and propagation of shear bands, highly localized in extremely narrow shear bands that nucleate and grow from shear transformation zones (STZs). Such highly localized deformation in BMGs typically causes catastrophic failure along a dominant shear band in tension. In an effort to overcome the problem of limited damage tolerance of BMGs at room temperature, various intrinsic and extrinsic approaches to multiply and/or hinder the propagation of individual shear bands have been explored in order to distribute the plastic strain over many shear bands. Intrinsic approaches include alloy modification [2,15–24], while use of composite structures provides an extrinsic approach [2,18,25–28].

There is a continuing interest in the mechanical characterization of BMGs. Uniaxial compression tests are often initially used with typical cylindrical sample dimensions of either 1 or 2 mm diameter with a length-to-diameter ratio of 2. The most common problem associated with

* Corresponding author. Tel.: +1 216 368 0583; fax: +1 216 368 3209.
E-mail address: xjgu2005@gmail.com (X.J. Gu).

compression testing of BMGs or other materials with low ductility are the sample dimensions where small cylinders are compressed between two parallel platens. The stress inhomogeneities and friction between the sample surface and the platens due to the imperfect plane parallelism in small samples can drastically alter the stress–strain response, leading to apparent compressive plasticity. Additional effects of constraint, alignment, lubrication, sample size, specimen aspect ratio, and the stiffness of the testing machine can similarly influence the plasticity of BMGs [29–35]. These various factors make it challenging to compare the amount of compressive plasticity of BMGs tested at different labs. It is also important to note, as will also be demonstrated in this paper, that compressive plasticity alone is not necessarily a good predictor of fracture toughness. Notched and/or fatigue pre-cracked samples tested in bending are an excellent way to evaluate toughness of BMGs, although care must be taken to ensure Mode I loading and details of the fatigue precracking must be considered in order to ensure reproducible results. Unlike uniaxial compression of BMGs that fail in shear under essentially mode II conditions, the triaxial tensile stress state present in fatigue pre-cracked three-point bending tests conducted under Mode I conditions is much more severe. However, the three-point bending test also has a size effect whereby smaller sized specimens display larger toughness. Sources of increased toughness include differences in crystallinity as well as plane strain to plane stress transitions in smaller sized samples [36].

Recently, Lewandowski and co-workers demonstrated a correlation between ν (or μ/B) and fracture energy for a range of BMG alloys as well as for annealing-induced embrittlement in terms of a competition between plastic flow and fracture [16,18]. It was found that the fracture toughness of BMGs was closely related to the ratio μ/B between the shear modulus (μ) and bulk modulus (B), or, equivalently, the Poisson's ratio ν . The μ/B ratios of tough BMGs were found to be <0.41 – 0.43 , or the Poisson's ratios >0.31 – 0.32 . All of the data in their paper were from specimens fractured in Mode I conditions. Schroers and Johnson reported that a Pt-based BMG with an unusually high Poisson's ratio of $\nu = 0.42$ (or low $\mu/B = 0.165$) can show large plastic strains in compression (20%) and bending ($>3\%$), with a very high notch fracture toughness ($K_{IC} \approx 80 \text{ MPa m}^{1/2}$) [15]. They also argued that a high Poisson's ratio (or small μ/B) can promote the formation of multiple shear bands and suppress crack initiation, which results in the observed large global plasticity and very high fracture toughness. Gu et al. recently investigated a $\text{Fe}_{65}\text{Mo}_{14}\text{C}_{15}\text{B}_6$ BMG doped with lanthanides to provide systematic changes to the elastic constants, and found that a well-defined transition from brittleness to plasticity in compression (i.e. essentially failing in shear as a mode II failure) was observed as Poisson's ratio approaches 0.32 from below (or μ/B drops to 0.41–0.42 from above) [37]. Fracture toughness experiments on a variety of Fe-based BMGs showed a similar trend [22].

The fracture mechanisms are different between mode I and mode II, as evidenced by the different fracture surface appearance and the different measured values of fracture angle and fracture toughness for these different test conditions [38,39]. For mode I failure, the correlation between ν (or μ/B) and fracture energy can be understood, at least qualitatively, in terms of a competition between the tendency for deformation in shear (μ) and for dilatation (B). With a low μ/B , the material prefers to deform plastically in shear rather than undergo the dilation necessary for fracture (e.g. for void nucleation and coalescence). Although the damage nucleation and coalescence process is different for mode II failure, it would be useful to directly compare the results obtained in these two different types of test (i.e. compression vs. fracture toughness) in order to determine if the critical value of ν (or μ/B) for plasticity/toughness of BMGs is universal or alloy system/deformation mode/testing condition dependent. To the author's knowledge, this has not been demonstrated on one alloy system. Such results would also provide some indication of the effects of stress state on plasticity/toughness. Previous studies on the correlation between elastic moduli and plasticity/toughness were performed in either mode II (compression test) [37,40] or mode I conditions [16,18,22] (three-point bending toughness test). To our knowledge, there is no systematic study on the correlation between elastic moduli and plasticity/toughness performed in both mode I and II conditions on the same material, and that is another part of the focus of this work.

In the present study, the effects of changes in cooling rate on the elastic moduli and deformation and fracture behavior in both toughness (mode I) and compression (mode II) conditions are presented. A strong correlation between elastic moduli and fracture for both mode I and mode II failures was established. We also report for the first time on a monolithic $\text{Ti}_{40}\text{Zr}_{25}\text{Cu}_{12}\text{Ni}_3\text{Be}_{20}$ BMG that shows a very high fracture toughness, approximately $110 \text{ MPa m}^{1/2}$, obtained from a fatigue pre-cracked specimen tested in three-point bending. The important roles of shear bands and test conditions that contribute to increased plasticity/toughness in this alloy are illustrated.

2. Experimental

The Ti-based bulk metallic glass (BMG) used in this investigation, $\text{Ti}_{40}\text{Zr}_{25}\text{Cu}_{12}\text{Ni}_3\text{Be}_{20}$ (at. pct), was developed by the University of Virginia and shows excellent glass forming ability (in the form of 5–10 g glassy ingot, or rod with diameter $>14 \text{ mm}$) [14]. $\text{Ti}_{40}\text{Zr}_{25}\text{Cu}_{12}\text{Ni}_3\text{Be}_{20}$ BMGs, in the form of rods with diameters from 1 to 3 mm, rectangular bars $5 \times 5 \text{ mm}^2$ in cross-section and ingots (10 g) were prepared using the methods described elsewhere [41]. The amorphous nature of the $\text{Ti}_{40}\text{Zr}_{25}\text{Cu}_{12}\text{Ni}_3\text{Be}_{20}$ samples was confirmed by X-ray diffraction and differential scanning calorimetry (DSC, Mettler Toledo DSC822^c) conducted at a heating rate of $20 \text{ }^\circ\text{C/min}$. Fig. 1 illustrates the essentially identical DSC traces for the sample sizes shown, with glass

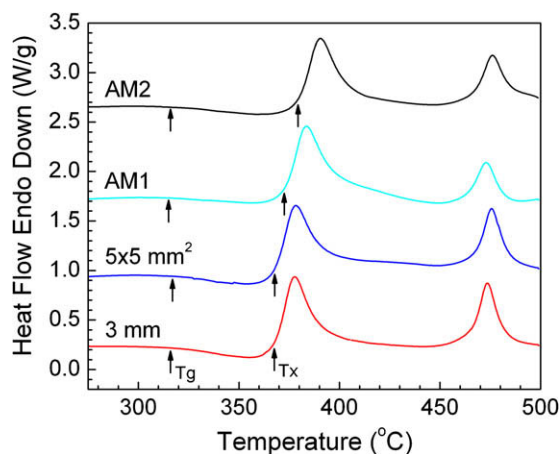


Fig. 1. DSC curves showing glass transition and crystallization for $d = 3$ mm, 5×5 mm², AM1 and AM2 Ti₄₀Zr₂₅Cu₁₂Ni₃Be₂₀ BMG samples.

transition temperature in the range of 315–317 °C and onset crystallization temperature in the range of 368–380 °C for those shown. The smaller diameter cylindrical samples were similarly amorphous while samples AM3 and AM4 were partially crystalline, as shown elsewhere [41].

Compression tests at room temperature were performed on an Instron 1125 load frame using cylindrical samples of 1, 2, or 3 mm diameter with an aspect ratio of ~ 2 and a 5×5 mm² rectangular bar with an aspect ratio of ~ 1.2 . The tests were done with an initial strain rate of 10^{-4} s⁻¹. A custom designed device was used to grind the ends of the specimens to ensure that the ends are flat and parallel and perpendicular to the lateral surfaces. The pulse-echo overlap technique with 10 MHz piezoelectric transducers was used to measure the shear and longitudinal wave speeds, enabling calculation of the elastic constants. Density measurements were carried out by Archimedes' principle. Both notch toughness and fatigue pre-cracked toughness tests were conducted. Three-point bend fracture toughness testing on the rectangular samples was conducted in general accordance with ASTM E399 on fatigue pre-cracked specimens of dimensions: B (thickness) = 5 mm, W (width) = 5 mm, and S (span) = 20 mm. The surfaces of the bend bar were carefully polished to a mirror finish to enable crack monitoring and examination after testing. All tests were carried out on a 20 Kip MTS model 810 closed loop servohydraulic testing machine. A fatigue precrack roughly 1 mm in length was initiated from the specimen with a notch root radius of 110 μ m, to a depth $a/W = 0.45$ at a load ratio (R) of 0.3 and at a test frequency of 15 Hz under decreasing ΔK condition (K control), using an automated load-shedding technique. The maximum ΔK level used in the fatigue cycle was 16.8 MPa m^{1/2}, while the minimum was approximately 10 MPa m^{1/2}, providing a maximum plane strain plastic zone size $2r_p$ ($r_p = K_c^2 / 6\pi\sigma_y^2$) during the fatigue precracking of 22 μ m and 8 μ m, respectively. This is well below the requirements outlined in ASTM E399. The crack length during precracking as

well as during the fracture toughness testing was measured using the direct current potential drop method (DCPD) and standard formula [42]. The three-point bend fracture toughness tests for the fatigue pre-cracked specimens were conducted at room temperature under displacement control with a rate of 0.1 mm min⁻¹. Scanning electron microscopy (SEM) was used to examine the fracture surfaces. An Olympus FV1000 laser-scanning confocal microscope (LSCM) in an upright configuration was used to characterize crack profile and surface topography of fracture surfaces. The scan head is fiber coupled to a Princeton Instruments 0.3 m spectrometer with a CCD detector.

3. Results and discussion

3.1. Uniaxial compression tests

Fig. 2a shows representative engineering stress–strain curves of Ti₄₀Zr₂₅Cu₁₂Ni₃Be₂₀ BMG cylindrical rods with diameters up to 3 mm and includes that for a 5×5 mm² rectangular bar tested under compressive loading, all taken

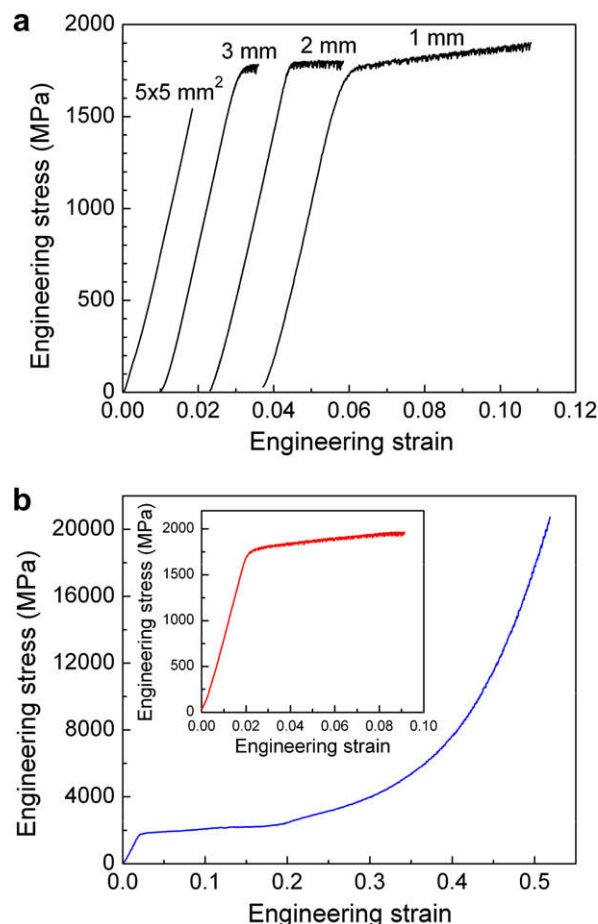


Fig. 2. (a) Representative engineering stress–strain curves of Ti₄₀Zr₂₅Cu₁₂Ni₃Be₂₀ BMG cylindrical rods with diameters up to 3 mm and that for a 5×5 mm² rectangular bar under compressive loading and (b) engineering compressive stress–strain curve of one of the 1 mm diameter cylindrical specimens. Inset shows the engineering stress–strain curve of a sample unloaded at 7% global plastic strain.

to complete separation of the samples into two distinct pieces. The compressive mechanical properties including 0.2% offset yield strength, engineering fracture strength and global plastic strain at failure are listed for all samples tested in Table 1. The present materials often exhibit fracture strengths exceeding ~ 1.7 GPa although both the strength and global compressive plastic strain at failure decreases with increasing sample size. As seen in Fig. 2a, the 5×5 mm² sample failed catastrophically at 1540 MPa without any macroscopic plastic strain while different amounts of strain and serrated flow were exhibited in nominally the same material when present as cylindrical rods with diameters ranging from 1 mm to 3 mm.

Close examination of additional separate tests on 1 mm diameter cylindrical specimens illustrates the plateau followed by the continuous load/engineering stress increase at very high strains as shown in Fig. 2b, similarly shown in other recent work [19]. SEM examination of this sample, Fig. 3a, clearly shows that the lateral sample surfaces are not perpendicular to the sample ends, and macro cracks span the sample after this large plastic deformation, Fig. 3b. Cracks were also observed on the topside of the deformed specimen, further confirming that failure had already occurred in this deformed sample, even though the engineering stress continued to increase as shown in Fig. 2b. Although dense shear bands were formed on the lateral surfaces of this highly deformed sample, a large number of cracks developed from the shear bands that formed in the early stages of plastic deformation. The shear slips and/or fractures on the subsidiary shear planes having different orientations with that of the primary shear bands, and their strong intersection and interaction with primary shear bands/fracture plane, resulted in the formation of serrated cracks/shear bands as also indicated (arrows) in Fig. 3b. Accordingly, the highly deformed specimen shown in Fig. 3a consisted of a large number of fractured components, which are mechanically bonded/welded. Microhardness measurements made on the top of the sample shown in Fig. 3a showed a slight hardness increase (i.e. from 499 ± 2.6 to 541 ± 4.5 kg/mm²) in this severely deformed

and unloaded sample (i.e. Fig. 2b), similar to other recent reports [19]. Separate DSC measurements on both the pristine and highly deformed sample also failed to reveal any significant differences in glass transition temperature and crystallization temperature.

In order to determine if fracture had occurred earlier in the stress–strain curve of Fig. 2b, another 1 mm diameter cylindrical sample was deformed in compression to 7% global plastic strain, unloaded, and examined in the SEM. The engineering stress strain curve for this interrupted test is shown in the inset to Fig. 2b. Fig. 3c clearly shows severe preferential deformation at the sample-to-platen edges in addition to extensive shear banding at both the sample ends and at intersections of the intense shear at the middle of the sample. The non-uniform deformation prevents calculation of the true stress–strain curve but does illustrate the heterogeneity of deformation both near the shear bands as well as at the sample-to-platen interfaces.

The present compression results clearly demonstrate that the Ti₄₀Zr₂₅Cu₁₂Ni₃Be₂₀ BMG undergoes a transition from apparent plasticity to brittleness when the sample dimensions approach a critical value. A specimen size effect on the compressive behavior and tendency for increased shear banding was also observed in other work on a Zr_{64.13}Cu_{15.75}Ni_{10.12}Al₁₀ BMG where the plasticity-to-brittleness transition occurred when the specimen size reached a critical sample size of 3 or 4 mm in diameter under a given machine stiffness [35]. The machine stiffness was measured in the present work as approximately 80,000 N/mm and the same experimental arrangement/machine stiffness was utilized for each experiment in order to eliminate this variable. This machine stiffness is in the higher range of those tested previously [35] and is not the primary source of the apparent plasticity changes amongst the present tests. Additional discussions regarding the other possible source(s) of the size effect observed in the present work are provided below.

The density, which decreases with increasing cooling rate during processing, substantially increases with increas-

Table 1
Measured density (ρ), microhardness (H_v), elastic constants (shear modulus μ , bulk modulus B , Young's modulus E and Poisson's ratio ν) and mechanical properties obtained from compression tests (0.2% offset yield stress $\sigma_{0.2}$, engineering fracture strength S_f , global plastic strain at failure e_p , fracture angle θ and calculated strain energy at fracture W) for Ti₄₀Zr₂₅Cu₁₂Ni₃Be₂₀ BMGs.

Sample size	ρ (g/cm ³)	H_v (kg/mm ²)	$\sigma_{0.2}$ (MPa)	S_f (MPa)	e_p (%)	μ (GPa)	B (GPa)	E (GPa)	ν	θ	W (MJ/m ³)
5×5 mm ²	5.391	505 \pm 4.6		1540	0	34.7 \pm 0.1	108.4 \pm 0.4	94.1 \pm 0.2	0.355 \pm 0.001	38	12.2
$d = 3$ mm	5.384	504 \pm 2.8	1760	1780	0.5	34.3 \pm 0.1	109.9 \pm 0.5	93.3 \pm 0.2	0.358 \pm 0.001	40	25.1
$d = 2$ mm	5.373	501 \pm 3.8	1790	1800	1.4	34.1 \pm 0.2	114.1 \pm 0.7	93.0 \pm 0.5	0.364 \pm 0.001	41	40.7
$d = 1$ mm	5.356	499 \pm 2.6	1720	1900	4.9	32.5 \pm 0.3	≥ 114.1		≥ 0.370	43	104.9
$d = 1$ mm	5.356		1790	2180	10	32.5 \pm 0.3	≥ 114.1		≥ 0.370		207.7
$d = 1$ mm ^a	5.356		1750		7	32.5 \pm 0.3	≥ 114.1		≥ 0.370		>144.3
2×2 mm ^{2b}	5.391		1710	1710	0.2	35.0 \pm 0.1	110.4 \pm 0.4	95.0 \pm 0.2	0.356 \pm 0.001	42	17.5
1×1 mm ^{2b}	5.391		1730	1790	1.6					42.5	43.8
1×1 mm ^{2b}	5.391		1710	1800	1.6					42.5	43.8
1×1 mm ^{2b}	5.391		1740	1860	3.5					43	78.8

^a Unloaded after 7% global plastic strain.

^b Machined from 5×5 mm² rectangular sample.

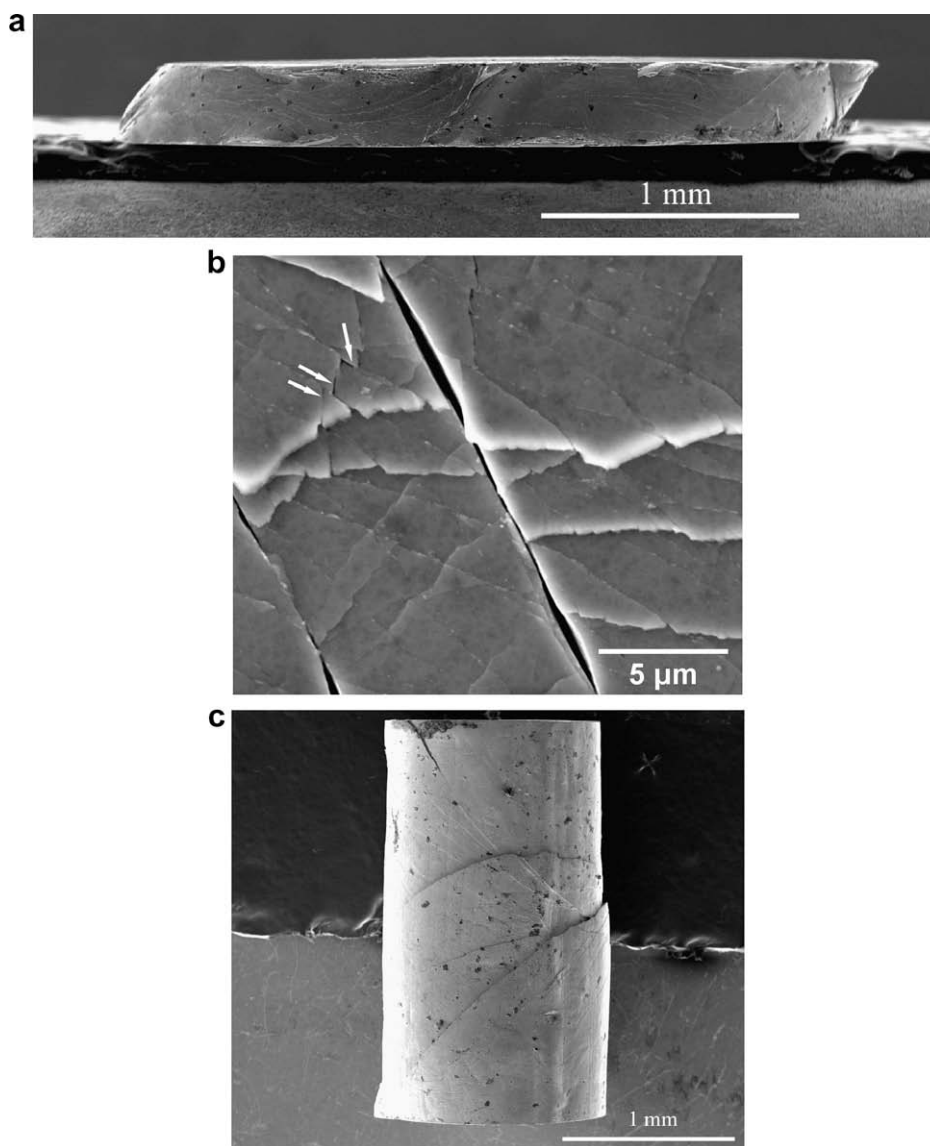


Fig. 3. SEM images of the 1 mm diameter cylindrical $\text{Ti}_{40}\text{Zr}_{25}\text{Cu}_{12}\text{Ni}_3\text{Be}_{20}$ BMG specimen subjected to large plastic deformation as shown in Fig. 2b: (a) side view; (b) high magnification view of lateral surface and (c) SEM view of separate 1 mm diameter sample unloaded after 7% plastic strain shown in inset to Fig. 2b.

ing sample dimension in the present material as seen in Table 1. The elastic constants of $\text{Ti}_{40}\text{Zr}_{25}\text{Cu}_{12}\text{Ni}_3\text{Be}_{20}$ BMGs subjected to the compression tests described above are also listed in Table 1. Only the shear modulus of the 1 mm diameter cylindrical sample is shown since the longitudinal wave speed of the 1 mm diameter samples could not be measured due to the limitation of the ultrasonic measurement system. Table 1 shows that the shear modulus (μ) and Young's modulus (E) decrease with decreasing sample size while bulk modulus (B) increases, producing an increasing Poisson's ratio with decreasing sample size. Combined with the results of the present compression tests, correlations between compressive plasticity and ν (or μ/B) provide another source of the sample size effect that is observed. The compressive plasticity of $\text{Ti}_{40}\text{Zr}_{25}\text{Cu}_{12}\text{Ni}_3\text{Be}_{20}$ BMG increases with increasing Poisson's ratio

(or decrease of μ/B). The $5 \times 5 \text{ mm}^2$ $\text{Ti}_{40}\text{Zr}_{25}\text{Cu}_{12}\text{Ni}_3\text{Be}_{20}$ BMG with a Poisson's ratio of 0.355 exhibits no compressive plasticity while the 1–3 mm diameter rods with higher Poisson's ratios show distinct plasticity under compressive loading, demonstrating the existence of an apparent critical Poisson's ratio (between 0.355 and 0.358) for compressive plasticity.

All compression samples failed in shear with a fracture angle of $38\text{--}43^\circ$. In contrast to the $5 \times 5 \text{ mm}^2$ sample, multiple shear banding was observed on the lateral surfaces of the smaller diameter cylindrical samples and the density of shear banding increased with decreasing sample size. A clear trend showing an increase of fracture angle with decreasing sample size was observed as shown in Table 1, although this is somewhat affected by the degree of plasticity in compression at failure.

Fig. 4 shows the fracture surfaces of two representative compression samples. All fractures initiated at one of the sample edges that met the compression platen as discussed later. Two kinds of features were observed on the fracture surfaces. The viscous river-like patterns (Fig. 4a) were formed along the shear direction near the fracture initiation site, followed by micrometer-scale features smeared in the direction of shear, Fig. 4b. The relatively large scale of the features on the fracture surface appears to be related to the toughness of this BMG system, as demonstrated later in this work as well as shown previously [43]. Regions near the fracture origin of samples exhibiting extensive compressive plasticity often exhibited profuse shear bands on the fracture surface along with the typical ridges of the river/vein patterns as shown in Fig. 4c.

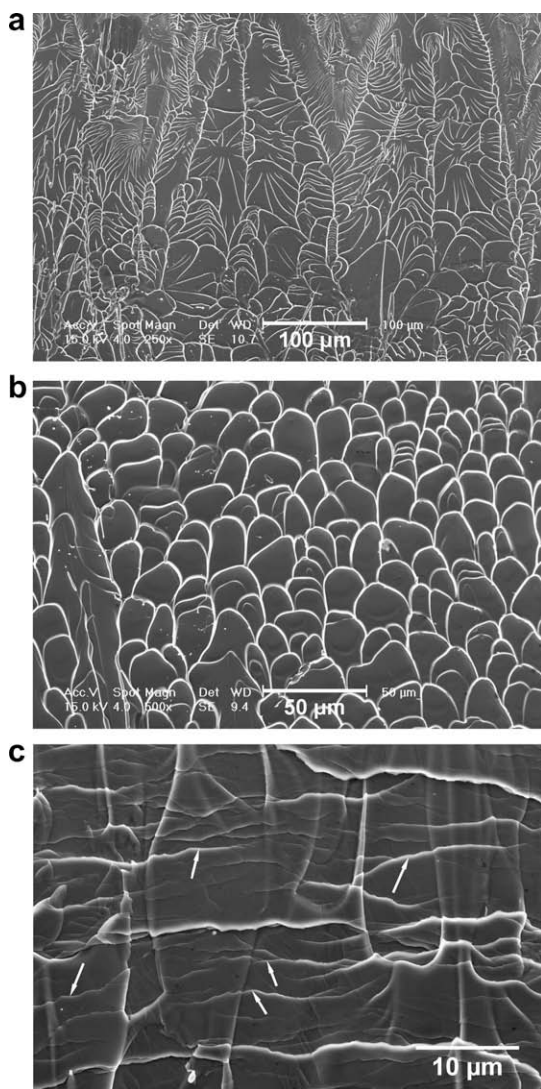


Fig. 4. SEM micrographs revealing the compressive fracture surfaces of $\text{Ti}_{40}\text{Zr}_{25}\text{Cu}_{12}\text{Ni}_3\text{Be}_{20}$ BMG: (a) viscous river-like patterns formed along the shear direction near fracture initiation site, (b) micrometer-scale features smeared in the direction of shear for $5 \times 5 \text{ mm}^2$ sample and (c) regions near the fracture origin of a 1 mm diameter cylindrical rod exhibiting extensive plasticity and evidence of intersecting shear (arrows) on the fracture surface.

3.2. Notched and fatigue pre-cracked toughness tests in mode I loading conditions

Fracture under mode I loading conditions typically produces failure at a critical stress intensity factor (K) that is smaller in magnitude compared to other loading geometries [39,54]. Fig. 5 replots the correlation between fracture energy and Poisson's ratio ν in mode I shown previously for this material [41], while the inset to Fig. 5 plots the normalized fracture energy with respect to the lowest notched fracture energy in order to illustrate the magnitude of change in fracture energy with increased Poisson's ratio. A strong correlation between fracture energy and ν (or μ/B) is again established where the fracture energy increases quite rapidly with increasing ν (or decreasing μ/B) with a distinct transition from brittle to tough behavior. The variation of elastic moduli in $\text{Ti}_{40}\text{Zr}_{25}\text{Cu}_{12}\text{Ni}_3\text{Be}_{20}$ BMG enabled the identification of a well-defined transition from brittleness to toughness. This transition occurs near a Poisson's ratio of 0.35, above which the $\text{Ti}_{40}\text{Zr}_{25}\text{Cu}_{12}\text{Ni}_3\text{Be}_{20}$ BMG is very tough, or a critical μ/B ratio of 0.33, below which the $\text{Ti}_{40}\text{Zr}_{25}\text{Cu}_{12}\text{Ni}_3\text{Be}_{20}$ BMG is very tough. This critical Poisson's ratio for the transition between brittleness and toughness in mode I conditions for $\text{Ti}_{40}\text{Zr}_{25}\text{Cu}_{12}\text{Ni}_3\text{Be}_{20}$ BMGs is somewhat lower than the apparent critical Poisson's ratio between 0.355 and 0.358 for compressive plasticity shown earlier for compressive failure that occurs under essentially mode II loading conditions. Interestingly, the $5 \times 5 \text{ mm}^2$ $\text{Ti}_{40}\text{Zr}_{25}\text{Cu}_{12}\text{Ni}_3\text{Be}_{20}$ BMG exhibits very high notch toughness (i.e. $102 \text{ MPa m}^{1/2}$) in mode I loading conditions in spite of the complete lack of global plasticity and low compressive fracture energy (to be discussed later) (c.f. Table 1, Fig. 2a). In order to further characterize the fracture behavior under more severe stress states and examine some of the sources of high toughness, fatigue pre-cracked samples of the $5 \times 5 \text{ mm}^2$ material were tested for fracture toughness.

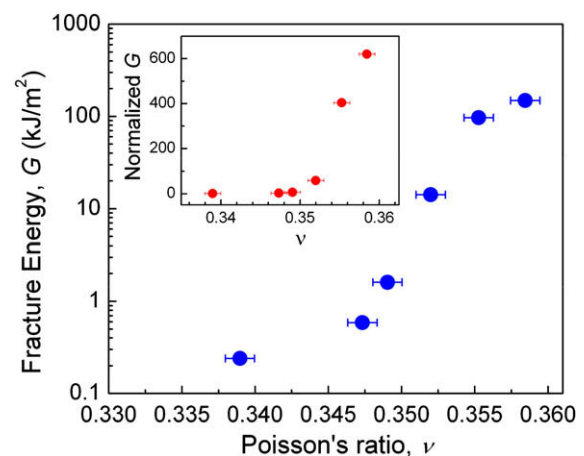


Fig. 5. Fracture energy G vs. Poisson's ratio ν for $\text{Ti}_{40}\text{Zr}_{25}\text{Cu}_{12}\text{Ni}_3\text{Be}_{20}$ BMGs listed in Table 1 in Ref. [41]. The inset to Fig. 5b plots the normalized fracture energy with respect to the lowest notched fracture energy shown.

The load vs. displacement traces for the $5 \times 5 \text{ mm}^2$ fatigue pre-cracked fracture toughness test and that of the notched (i.e. $110 \mu\text{m}$ root radius) toughness test sample were essentially the same (i.e. similar fracture load). In addition to some non-linearity in the load–displacement trace, the fracture toughness of the fatigue pre-cracked $5 \times 5 \text{ mm}^2$ $\text{Ti}_{40}\text{Zr}_{25}\text{Cu}_{12}\text{Ni}_3\text{Be}_{20}$ BMG was found to be $110 \text{ MPa m}^{1/2}$, somewhat higher than that obtained on the notched toughness test of identical dimensions (i.e. $102 \text{ MPa m}^{1/2}$). A stable crack growth region of only $40 \mu\text{m}$ was detected by DCPD method for the fatigue pre-cracked test.

3.3. Comparison of compression tests to notched/pre-cracked toughness tests

The present results clearly show a positive effect of increasing the Poisson's ratio on both the compressive plasticity and fracture energy measured under both notched bending and fatigue pre-cracked conditions. In the compression experiments, increased compressive plasticity was obtained for smaller diameter/thickness samples. At least two factors contribute to this observation. While various works have shown the benefits of increasing Poisson's ratio on the compressive plasticity of BMGs [37,40], various other works have also shown significant effects of test conditions/stress concentrations and sample thickness/size on strength and observations of (compressive) plasticity [29–35].

The present results illustrate that larger samples display lower Poisson's ratio and higher density for essentially the same chemistry. The slower cooling rate accompanying the larger samples produced substantial changes to the density and Poisson's ratio, indicative of a more relaxed structure in the slower cooled and denser materials. The increase of shear modulus with decreasing cooling rates observed in the present study can be understood as a decrease of the concentration of structural defects induced by structural relaxation of metallic glasses [44]. Recently, Pan et al. reported that the ductility of BMGs was found to intrinsically correlate with their shear transformation zone volumes [45]. Experimentally, they observed that the measured STZ volumes increase with increasing Poisson's ratio and BMG ductility. The STZs with a large size reinforce the shear capability of the metallic glass and promote the formation of multiple shear bands, which is consistent with the current findings that the compressive plasticity increases with increasing Poisson's ratio. While the lower Poisson's ratio clearly compromises the compressive plasticity to the extent that the $5 \times 5 \text{ mm}^2$ rectangular samples failed in the elastic regime, the hardness results showed in Table 1 reveal slightly higher hardness and more scatter in the $5 \times 5 \text{ mm}^2$ sample, also suggesting a sample geometry/size effect on plasticity, as seen by others [32,35].

Another important source of such observations of differences in compressive plasticity are stress concentrations and alignment issues. As shown by Sunny et al. [29,30] and Wu et al. [31], changes to both the strength and

compressive plasticity are possible via effects of misalignment and stress concentrations between the compression platens and samples. Although the present samples were machined and polished to be flat and parallel while using an alignment fixture for testing, the differences in sample diameter along with the mismatch in properties from compression platens to sample has been shown to create stress concentrations at the sample to platen interface, which manifest themselves in the manner shown in Fig. 3c. All compression samples exhibited eventual fracture which emanated from one edge of the sample corresponding to the platen to sample interface. This was particularly evident in the $5 \times 5 \text{ mm}^2$ rectangular sample that exhibited zero compressive plasticity and lower strength (despite its slightly higher hardness) than the cylindrical samples which exhibited evidence of shear band initiation and growth from edges in contact with the platen. Nonetheless, the thinner samples did exhibit evidence of increasing compressive plasticity with increasing Poisson's ratio on going from the $5 \times 5 \text{ mm}^2$ sample to the 1 mm diameter cylindrical samples. Perhaps most surprising is the complete lack of compressive plasticity in the $5 \times 5 \text{ mm}^2$ rectangular compression sample in contrast to the exceptional notched and fatigue pre-cracked fracture toughness/energy results.

In order to examine these effects more fully, the $5 \times 5 \text{ mm}^2$ sample was machined into multiple compression samples with smaller cross-sections (i.e. $2 \times 2 \text{ mm}^2$ and $1 \times 1 \text{ mm}^2$) and an aspect ratio of 2. Table 1 includes all the compression data on these smaller samples taken directly from the $5 \times 5 \text{ mm}^2$ samples, while Fig. 6 summarizes the typical results. It is clear that smaller samples machined from the same $5 \times 5 \text{ mm}^2$ rectangular bar exhibit different amounts of compressive plasticity and strength without a significant difference in Poisson's ratio, as shown by the $2 \times 2 \text{ mm}^2$ sample (c.f. Table 1, Fig. 6) and inferred by the behavior of the $1 \times 1 \text{ mm}^2$ samples. Measurements of ν in the $1 \times 1 \text{ mm}^2$ samples was not possible due to size limitations. Deformation and fracture in all cases emanated from the

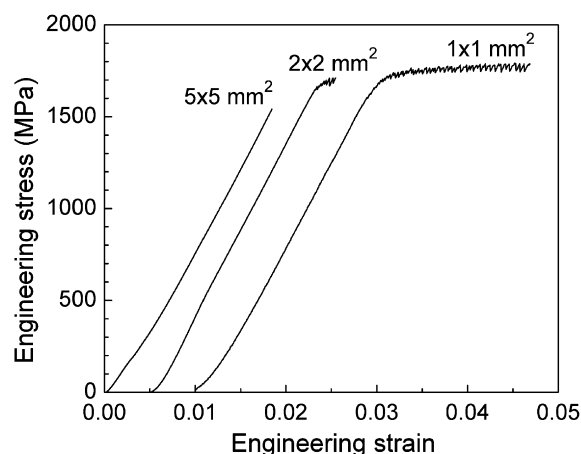


Fig. 6. Representative engineering stress–strain curves of rectangular $\text{Ti}_{40}\text{Zr}_{25}\text{Cu}_{12}\text{Ni}_3\text{Be}_{20}$ BMG bar samples with different cross-sections. The $2 \times 2 \text{ mm}^2$ and $1 \times 1 \text{ mm}^2$ samples were machined directly from the $5 \times 5 \text{ mm}^2$ samples.

edges of the samples, as shown in the present and previous work [29–31], although more deformation near the edges of the samples (i.e. which is reflected in greater compressive deflection) was exhibited in the smaller samples. Although all of these samples were tested at the same L/D ratio but with different sizes, the smaller sized samples will experience a higher compressive confinement/constraint, as shown in early work on semi-brittle materials. Higher compressive confinement/constraint has been shown to increase the compressive plasticity of a Zr-based bulk metallic glass in previous work [46,47], and appears to be another source of the increased compressive plasticity that accompanies the smaller samples in the present work. A similar size effect was recently reported in $\text{Zr}_{52.5}\text{Ni}_{14.6}\text{Al}_{10}\text{Cu}_{17.9}\text{Ti}_5$ BMG and ascribed to the critical shear offset and the energy density dissipated on the shear fracture surface caused by the elastic energy release [33].

Fig. 7 summarizes the strain energy at compressive fracture (Table 1) calculated from the area under the compressive stress–strain curve for the rods with diameters up to

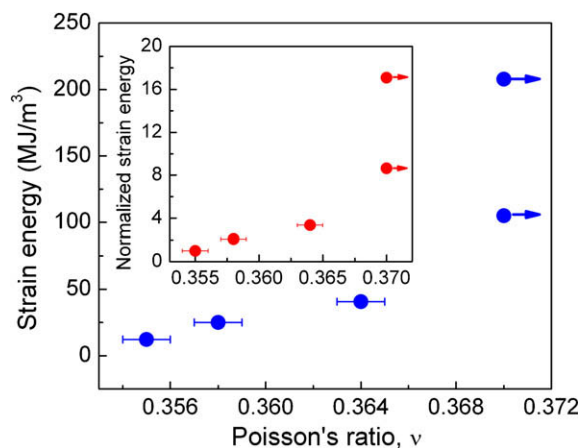


Fig. 7. Compressive strain energy at fracture vs. Poisson's ratio ν for $\text{Ti}_{40}\text{Zr}_{25}\text{Cu}_{12}\text{Ni}_3\text{Be}_{20}$ BMG cylindrical rods with diameters up to 3 mm and a $5 \times 5 \text{ mm}^2$ rectangular bar. The inset plots the normalized strain energy with respect to the lowest compressive strain energy for samples tested.

3 mm and the $5 \times 5 \text{ mm}^2$ sample. The inset to Fig. 7 plots the normalized strain energy (i.e. with respect to the lowest value) at failure for subsequent comparison to the toughness values. Values for ν had to be estimated for the 1 mm diameter samples since only μ and not B could be obtained. An increasing trend of bulk modulus with decreasing sample diameter was inferred, providing $\nu \geq 0.370$ for the 1 mm diameter samples, represented as arrows in Fig. 7. The critical Poisson's ratio for compressive plasticity in $\text{Ti}_{40}\text{Zr}_{25}\text{Cu}_{12}\text{Ni}_3\text{Be}_{20}$ BMGs is somewhat higher than the critical Poisson's ratio 0.32 for plasticity in Fe-based BMGs under compressive loading [37]. Combined with the fact that the lack of compressive plasticity was observed in some Zr- [48], Cu- [49], and rare earth-based [50] BMGs with ν as high as $\sim 0.35\text{--}0.375$, the results also suggest that different BMG systems may show different critical Poisson's ratios for compressive plasticity, although the amount of compressive plasticity is also clearly affected by sample dimensions and test technique, as discussed above. The normalized plots for strain energy at fracture in compression, Fig. 7, and the normalized plot for fracture energy in notched bending, Fig. 5, both illustrate the large effects of changes in Poisson's ratio. However, the magnitude of the effect is significantly greater in the notch toughness results (e.g. $620\times$ improvement in toughness vs. $8\text{--}17\times$ improvement in strain energy at fracture, discussed below).

Review of the results obtained on the toughness samples provides a similar size effect, in addition to a significant toughness in samples that exhibited essentially zero compressive plasticity (Table 2). Furthermore, for exactly the same sample composition the fracture energy increase from the least tough (0.2 kJ m^{-2} for the sample AM4 with a Poisson's ratio of 0.339) to most tough (148.9 kJ m^{-2} for the 3 mm diameter rod with a Poisson's ratio of 0.358) exceeded $620\times$ improvement [41]. In addition, the fatigue pre-cracked sample exhibited an exceptionally high toughness (e.g. $110 \text{ MPa m}^{1/2}$) that was slightly higher than that obtained on a notched sample (e.g. $102 \text{ MPa m}^{1/2}$). Additional observations and possible sources of such behavior are discussed below.

Table 2

Test conditions, fracture toughness (K_{IC}), yield stress σ_y ($=H_v/3$), plane strain plastic zone radius r_p , critical thickness $B = 2.5(K_{\text{IC}}/\sigma_y)^2$, stress state and Poisson's ratio ν for $\text{Ti}_{40}\text{Zr}_{25}\text{Cu}_{12}\text{Ni}_3\text{Be}_{20}$ BMGs.

Sample size	Condition	K_{IC} ($\text{MPa m}^{1/2}$)	σ_y (MPa)	r_p (μm)	B_{crit} (mm)	Stress state	ν
$5 \times 5 \text{ mm}^2$	Fatigue pre-cracked	110	1651	235	11.1	Mixed plane σ/ε	0.355 ± 0.001
$5 \times 5 \text{ mm}^2$	Fatigued to failure	98.6	1651	189	8.9	Mixed plane σ/ε	0.355 ± 0.001
$5 \times 5 \text{ mm}^2$	Notched	102.2	1651	203	9.6	Mixed plane σ/ε	0.355 ± 0.001
$d = 3 \text{ mm}$	Notched	126.3	1648	312	14.7	Mixed plane σ/ε	0.358 ± 0.001
$d = 1 \text{ mm}^a$	Notched	>59.8	1631				
$4 \times 6 \times 24 \text{ mm}^3$ (AM1 ^b)	Notched	39.7	1677	30	1.4	Plane ε	0.352 ± 0.001
$4 \times 6 \times 24 \text{ mm}^3$ (AM2 ^b)	Notched	13.5	1706	3.3	0.16	Plane ε	0.349 ± 0.001
$4 \times 6 \times 24 \text{ mm}^3$ (AM3 ^b)	Notched	8.2	1746	1.1	0.06	Plane ε	0.347 ± 0.001
$4 \times 6 \times 24 \text{ mm}^3$ (AM4 ^b)	Notched	5.4	1935	0.3	0.02	Plane ε	0.339 ± 0.001

^a Bent without failure.

^b Ref. [41] provides definition of AM1, AM2, AM3 and AM4.

It has been clearly demonstrated in previous work that for the Zr–Ti–Cu–Ni–Be BMG system that the three-point bend fatigue pre-cracked fracture toughness is significantly less than that obtained on notched samples containing different notch root radii [21,51]. However, the present results on this exceptionally tough $\text{Ti}_{40}\text{Zr}_{25}\text{Cu}_{12}\text{Ni}_3\text{Be}_{20}$ BMG illustrate a relatively minor effect of notch radius on going from 110 μm to a fatigue precrack. In fact, the fatigue pre-cracked sample exhibits a larger toughness (i.e. 110 $\text{MPa m}^{1/2}$) than the notched sample (i.e. 102 $\text{MPa m}^{1/2}$). Macroscopic side views of the notched and fatigue pre-cracked samples tested to failure in Fig. 8a and b respectively show the possible sources of this observation, while also providing evidence of the exceptional fracture toughness/energy in spite of the complete lack of compressive plasticity in

the $5 \times 5 \text{ mm}^2$ $\text{Ti}_{40}\text{Zr}_{25}\text{Cu}_{12}\text{Ni}_3\text{Be}_{20}$ BMG. Both Fig. 8a and b show excessive shear banding emanating from the notch and fatigue precrack, to the extent of classic general yielding coincident with fracture in the latter, reminiscent of early work and similar observations by Masumoto et al. on Pd-based glasses [52]. The extensive shear banding in both the notched and fatigue pre-cracked samples provides one source of the high toughness, while the extensive blunting of the fatigue precrack tip provided by the shear banding and formation of the plastic ‘hinges’ shown in Fig. 8b produces an effective notch radius that is actually larger than that in the notched sample shown in Fig. 8a. SEM measurements of the crack-tip opening displacement (CTOD) in the latter reveal 110 μm in comparison to the notch radius of 110 μm . While the extensive shear banding at the fatigue precrack tip produces an effective crack tip radius that is actually similar to the notched sample, the formation of the ‘hinge’ in Fig. 8b enables additional rotation and produces general yielding in the fatigue pre-cracked sample. Table 2 further shows that these high toughness samples are in a mixed plane stress/plane strain stress state, also known to inflate the toughness values [36]. An identical $5 \times 5 \text{ mm}^2$ sample was notched to $a/W = 0.14$ with a notch root radius of 110 μm and fatigued to failure at a load ratio of 0.3 and at a test frequency of 15 Hz using a starting $\Delta K = 25.6 \text{ MPa m}^{1/2}$. The sample failed upon reaching a $K_c = K_{\text{max}} = 98.6 \text{ MPa m}^{1/2}$ with a final crack length of $a/W = 0.5$. Fig. 9 shows the outside surface of this sample revealing the lack of the general yielding exhibited by the fatigue pre-cracked sample tested under quasi-static conditions shown in Fig. 8b.

The observations on the fatigue pre-cracked sample tested under quasi-static conditions (Fig. 8b) are somewhat analogous to that shown previously for a fatigue pre-cracked single edge notched bend sample of Zr-based glass tested in tension [53], although these are absent in the sample fatigued to failure (Fig. 9). The extensive shear banding further bifurcates the crack and provides mixed mode loading, also known to produce significant increases to the toughness of BMGs [54]. This also suggests that the notch radius effect clearly documented for the Zr-based BMG in early work [18,21,51] may be different for different BMGs and may depend on the Poisson’s ratio and its effects on the extent of shear banding, as discussed further below.

Similar to previous work [43], Fig. 10 also shows a clear correlation between the fracture surface feature sizes in the overload region and the magnitude of toughness, with the

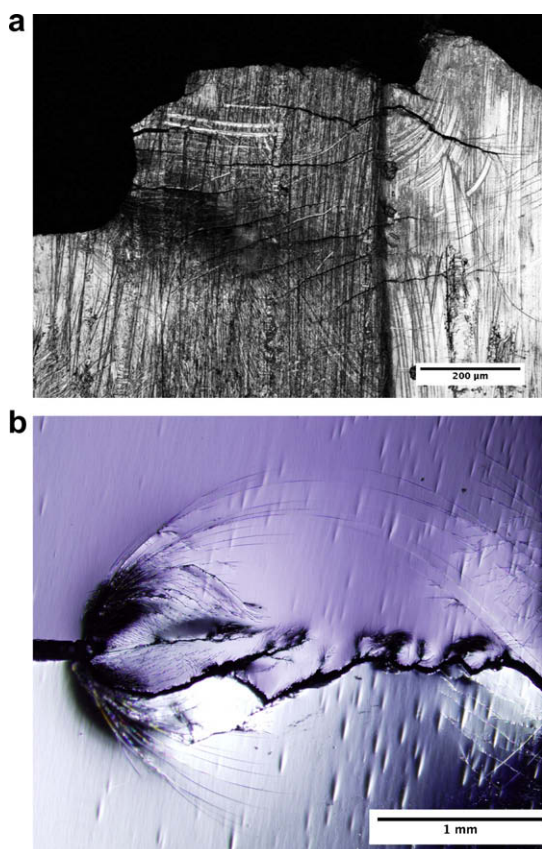


Fig. 8. Laser scanning confocal microscopy (LSCM) images showing the macroscopic side views of the notched (a) and fatigue pre-cracked (b) $5 \times 5 \text{ mm}^2$ $\text{Ti}_{40}\text{Zr}_{25}\text{Cu}_{12}\text{Ni}_3\text{Be}_{20}$ BMG samples tested to failure.

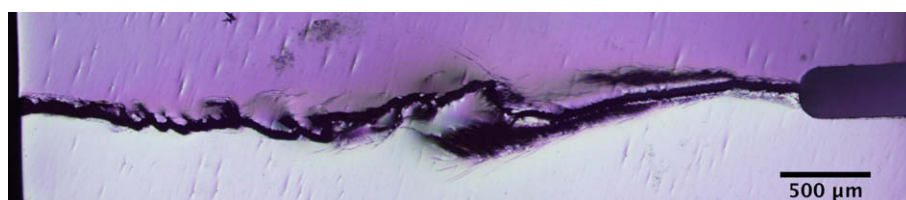


Fig. 9. LSCM image showing the macroscopic side view of the $5 \times 5 \text{ mm}^2$ sample fatigued to failure.

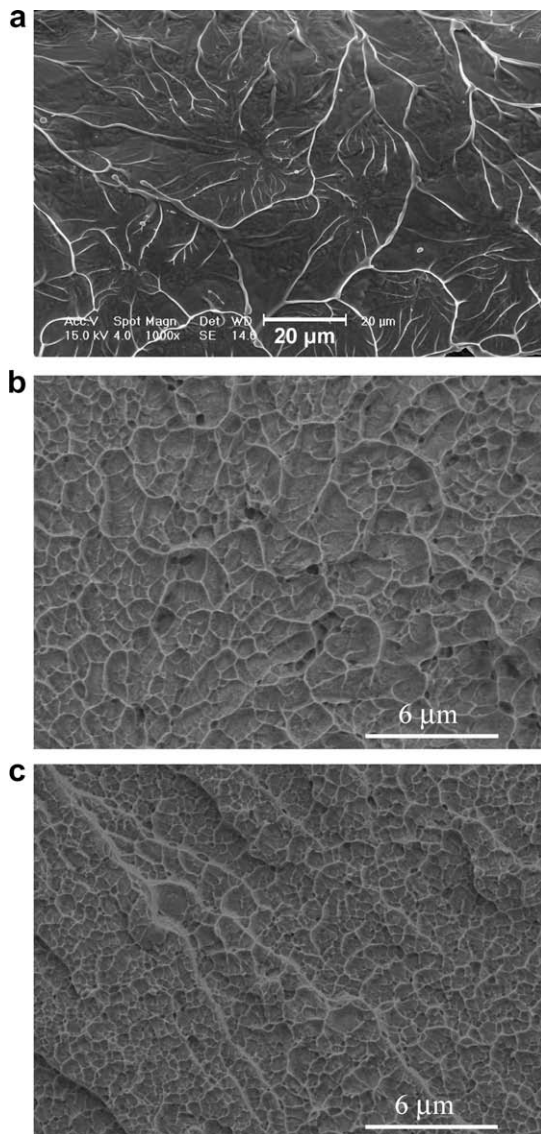


Fig. 10. SEM images of fracture surfaces in the overload region of the $\text{Ti}_{40}\text{Zr}_{25}\text{Cu}_{12}\text{Ni}_3\text{Be}_{20}$ BMGs with different notch toughness values: (a) $126.3 \text{ MPa m}^{1/2}$; (b) $39.7 \text{ MPa m}^{1/2}$ and (c) $8.2 \text{ MPa m}^{1/2}$.

least tough samples (i.e. lowest Poisson's ratio of 0.347) shown in Fig. 10c and the toughest (i.e. highest Poisson's ratio of 0.358) shown in Fig. 10a. The vein pattern size for the 3 mm diameter $\text{Ti}_{40}\text{Zr}_{25}\text{Cu}_{12}\text{Ni}_3\text{Be}_{20}$ BMG ($K_{\text{IC}} = 126.3 \text{ MPa m}^{1/2}$) is in the range of several tens of micrometers as shown in Fig. 10a while the vein pattern size for the specimen with a K_{IC} of $39.7 \text{ MPa m}^{1/2}$ significantly drops to several micrometers (Fig. 10b) and much finer scale (e.g. sub-micrometer) is observed for the sample with a K_{IC} of $8.2 \text{ MPa m}^{1/2}$ (Fig. 10c). The correlation between the vein pattern size and notch toughness can be explained in terms of the viscosity change in the shear band upon fracture. A separate study on the effects of viscosity on flow and fracture behavior of various model viscous fluids also shows that an increasing viscosity decreases the feature size on the fracture surfaces [55], which is consistent with the present findings. In addition to differences in the

fracture surface features sizes which scale with the Poisson's ratio, the extent of the planar zone emanating from the notch/precrack also scales with the Poisson's ratio, as shown in previous work [41].

The source of the planar zone that emanates from the notch appears to be due to the intense shear that occurs along the intense slip lines of the material, shown earlier in Fig. 8a for the notched $5 \times 5 \text{ mm}^2$ sample. Matching surface stereo-SEM fractographs in Fig. 11 reveal features from opposite sides of the notch which appear on the fracture surface. The stereo-image in Fig. 11a shows the notch region (left hand side) followed by the planar fracture region. On the planar fracture region appears four distinct raised portions (arrowed) that exhibit features of the notch. However, examination of the matching fracture surface and notch in Fig. 11b reveals that these four features are remnants from the other side of the notch. This is more clearly revealed by conducting laser-scanning confocal microscope of the matching surfaces in these regions. Fig. 12a corresponds to that shown in Fig. 11a while Fig. 12b corresponds to that shown in Fig. 11b. The intense shear which emanates from the various positions along the notch, eventually creating the fracture surfaces shown, intersect to produce the fracture surface features on opposite sides of the fracture surfaces shown in Figs. 11a, b and 12a, b. Evidence of intense shear band offsets on the fracture surfaces in the overload regions were also observed (arrowed), as shown in Fig. 13, indicative of the intersections of intense shear bands with the fracture surface.

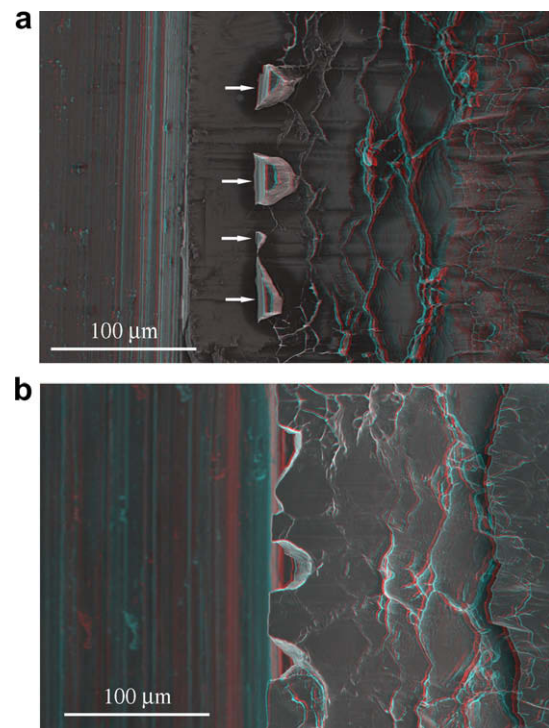


Fig. 11. Matching fracture surfaces (a) and (b) of the $5 \times 5 \text{ mm}^2$ notched toughness test $\text{Ti}_{40}\text{Zr}_{25}\text{Cu}_{12}\text{Ni}_3\text{Be}_{20}$ BMG sample observed as a stereo pair from the SEM.

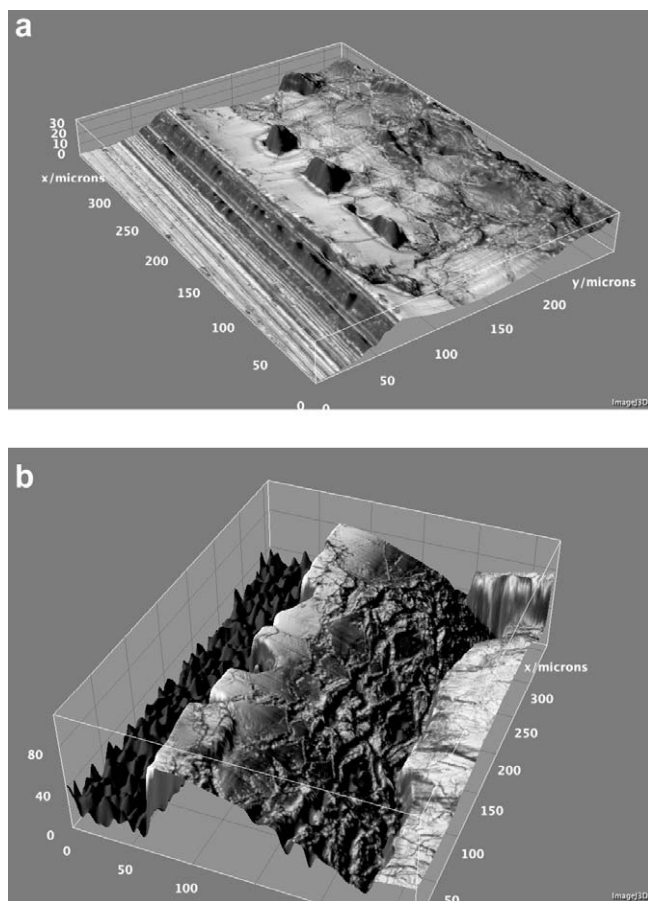


Fig. 12. Opposite fracture surface topographies (a) and (b) of the $5 \times 5 \text{ mm}^2$ notched toughness test $\text{Ti}_{40}\text{Zr}_{25}\text{Cu}_{12}\text{Ni}_3\text{Be}_{20}$ BMG sample observed through LSCM.

Other recent work has similarly shown a beneficial effect of increasing Poisson's ratio on both the compressive plasticity [37] and notch toughness [22]. Although the levels of compressive plasticity and notch toughness in the Fe-based BMGs were substantially less than that found in the pres-

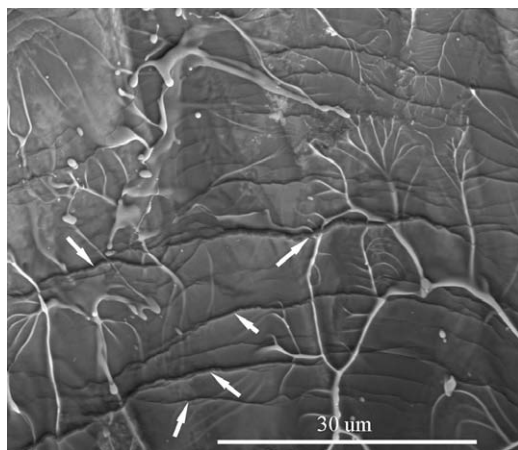


Fig. 13. SEM micrograph of fracture surface in the overload region of the $5 \times 5 \text{ mm}^2$ notched toughness test $\text{Ti}_{40}\text{Zr}_{25}\text{Cu}_{12}\text{Ni}_3\text{Be}_{20}$ BMG sample showing shear band intersections (arrowed) with the fracture surface.

ent Ti-based BMGs, the Fe-based BMGs have significantly lower Poisson's ratio, consistent with the general trend shown earlier [15,16,18] that correlates the general level of toughness with changes in Poisson's ratio. In order to compare this earlier Fe-based BMG work with the present Ti-based BMG work, Fig. 14a and b replot the earlier data on the Fe-based BMGs for both the strain energy at fracture in compression and the notch fracture energy, respectively. Included in the insets to both plots are the normalized values with respect to the lowest values reported in those works. Consistent with the present work, the normalized notch toughness values show significantly greater levels of improvement in comparison to the normalized compressive strain energy at fracture, although the normalized values for the Fe-based BMGs are significantly less than that demonstrated presently for the Ti-based BMGs. The Fe-based BMGs similarly revealed changes to the fracture surface morphology/size scale with increasing Poisson's ratio/toughness, again suggesting that changes to the Poisson's ratio affect the glass viscosity and such features. Furthermore, attempts at conducting fatigue pre-cracked tests on the Fe-based BMGs revealed signifi-

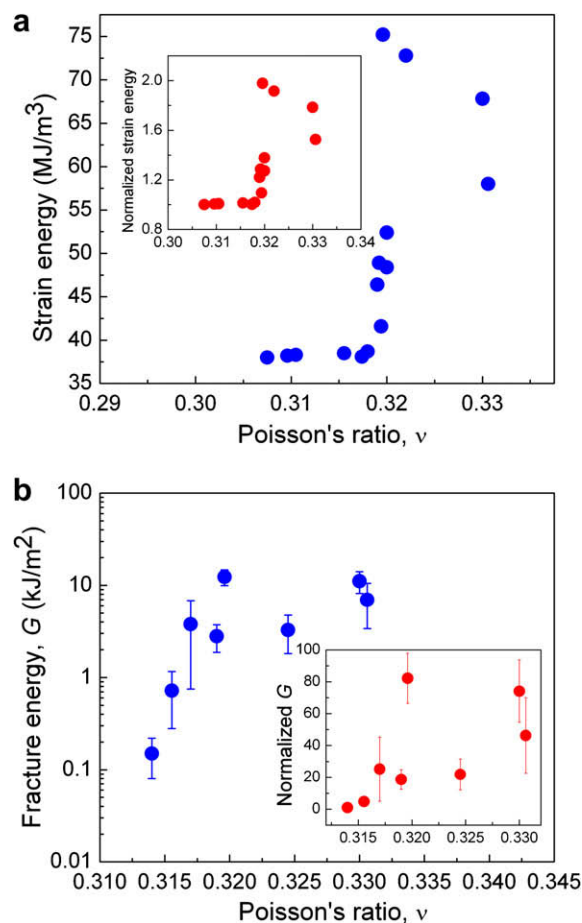


Fig. 14. Strain energy at fracture in compression (a) and notch fracture energy G (b) vs. Poisson's ratio ν for a variety of Fe-based BMGs. Included in the insets to both plots are the normalized values with respect to the lowest values reported in earlier work [22].

cant decreases to the fatigue pre-cracked toughness in comparison to that observed presently on the Ti-based BMG [56]. This again emphasizes the important point that the notch radius/size effect may be different in different BMGs and dependent on the Poisson's ratio as well as any other extrinsic (e.g. inclusions, porosity, etc.) that might serve as potent fracture initiation sites, also shown in previous work on the Fe-based BMGs [57].

One other contributing factor on the magnitude of toughness relates to the effects of plane strain vs. plane stress. All of the Fe-based BMGs fail under nominally plane strain conditions, while Table 2 previously revealed that most of the Ti-based BMGs fail under plane strain conditions except that the 3 mm diameter rod and $5 \times 5 \text{ mm}^2$ bar fail under a mixture of plane stress and strain.

4. Conclusions

The effects of changes in sample size and stress state on the compressive plasticity and fracture energy of $\text{Ti}_{40}\text{Zr}_{25}\text{Cu}_{12}\text{Ni}_3\text{Be}_{20}$ BMG were determined. Increases in sample size from 1 mm diameter rods to $5 \times 5 \text{ mm}^2$ rectangular bars increased the density while decreasing the Poisson's ratio. These increased sample dimensions produced decreases to the compressive plasticity, consistent with the expected effects of decreased Poisson's ratio. However, machining smaller samples from the same $5 \times 5 \text{ mm}^2$ bar also produced increased compressive plasticity without significantly changing the Poisson's ratio. This also confirms the important effects of sample geometry on magnitude of compressive plasticity. Furthermore, both notched and fatigue pre-cracked samples of identical dimensions revealed that the $5 \times 5 \text{ mm}^2$ rectangular bars exhibited exceptional toughness and fracture energy without exhibiting any compressive plasticity. Examination of failed toughness samples revealed significant shear banding in both notched and fatigue pre-cracked samples, with the extent of shear banding in the fatigue pre-cracked sample sufficient to produce general yielding. This highlights some of the inherent differences between compression testing and (notch/fatigue precrack) toughness testing as well as some of the test sample/geometry factors contributing to plasticity and toughness in these systems. It is clearly shown that large differences and significant fracture energies are possible between samples which exhibit limited compressive/tensile plasticity, even for samples fractured under plane strain conditions. The critical Poisson's ratio for plasticity/toughness is also affected by details of the test technique.

Acknowledgements

The research is supported by the DARPA Structural Amorphous Metals Program under ONR Grant No. N00014-06-1-0492. The assistance of Prof. D. Schuele with elastic constants measurements and Dr. D. Hovis with

LSCM is gratefully acknowledged. The document is approved for public release, distribution unlimited.

References

- [1] Schuh CA, Hufnagel TC, Ramamurty U. *Acta Mater* 2007;55:4067.
- [2] Greer AL. *Mater Today* 2009;12:14.
- [3] Yavari AR, Lewandowski JJ, Eckert J. *MRS Bull* 2007;32:635.
- [4] Farmer J, Choi JS, Saw C, Haslam J, Day D, Hailey P, et al. *Metall Mater Trans A* 2009;40:1289.
- [5] Peker A, Johnson WL. *Appl Phys Lett* 1993;63:2342.
- [6] Inoue A, Zhang T, Nishiyama N, Ohba K, Masumoto T. *Mater Trans JIM* 1993;34:1234.
- [7] Inoue A, Nishiyama N, Kimura H. *Mater Trans JIM* 1997;38:179.
- [8] Guo FQ, Poon SJ, Shiflet GJ. *Appl Phys Lett* 2003;83:2575.
- [9] Ma H, Shi LL, Xu J, Li Y, Ma E. *Appl Phys Lett* 2005;87:181915.
- [10] Ponnambalam V, Poon SJ, Shiflet GJ. *J Mater Res* 2004;19:1320.
- [11] Lu ZP, Liu CT, Thompson JR, Porter WD. *Phys Rev Lett* 2004;92:245503.
- [12] Xu DH, Duan G, Johnson WL. *Phys Rev Lett* 2004;92:245504.
- [13] Shen Y, Ma E, Xu J. *J Mater Sci Technol* 2008;24:149.
- [14] Guo FQ, Wang H-J, Poon SJ, Shiflet GJ. *Appl Phys Lett* 2005;86:091907.
- [15] Schroers J, Johnson WL. *Phys Rev Lett* 2004;93:255506.
- [16] Lewandowski JJ, Wang WH, Greer AL. *Philos Mag Lett* 2005;85:77.
- [17] Das J, Tang MB, Kim KB, Theissmann R, Baier F, Wang WH, et al. *Phys Rev Lett* 2005;94:205501.
- [18] Lewandowski JJ, Shazly M, Nouri AS. *Scripta Mater* 2006;54:337.
- [19] Liu YH, Wang G, Wang RJ, Zhao DQ, Pan MX, Wang WH. *Science* 2007;315:1385.
- [20] Gu XJ, Poon SJ, Shiflet GJ, Widom M. *Acta Mater* 2008;56:88.
- [21] Lewandowski JJ. *Mater Trans JIM* 2001;42:633.
- [22] Lewandowski JJ, Gu XJ, Nouri AS, Poon SJ, Shiflet GJ. *Appl Phys Lett* 2008;92:091918.
- [23] Zhang L, Cheng YQ, Cao AJ, Xu J, Ma E. *Acta Mater* 2009;57:1154.
- [24] Kim CP, Suh JY, Wiest A, Lind ML, Conner RD, Johnson WL. *Scripta Mater* 2009;60:80.
- [25] Hofmann DC, Suh JY, Wiest A, Duan G, Lind ML, Demetriou MD, et al. *Nature* 2008;451:1085.
- [26] Guo FQ, Poon SJ, Shiflet GJ. *Philos Mag Lett* 2008;88:615.
- [27] Hofmann DC, Suh JY, Wiest A, Lind ML, Demetriou MD, Johnson WL. *Proc Natl Acad Sci USA* 2008;105:20136.
- [28] Launey ME, Hofmann DC, Johnson WL, Ritchie RO. *Proc Natl Acad Sci USA* 2009;106:4986.
- [29] Sunny G, Yuan F, Prakash V, Lewandowski J. *Exp Mech* 2009;49:479.
- [30] Sunny G, Lewandowski J, Prakash V. *J Mater Res* 2007;22:389.
- [31] Wu WF, Li Y, Schuh CA. *Philos Mag* 2008;88:71.
- [32] Huang YJ, Shen J, Sun JF. *Appl Phys Lett* 2007;90:081919.
- [33] Wu FF, Zhang ZF, Mao SX, Eckert J. *Philos Mag Lett* 2009;89:178.
- [34] Bei H, Xie S, George EP. *Phys Rev Lett* 2006;96:105503.
- [35] Han Z, Wu WF, Li Y, Wei YJ, Gao HJ. *Acta Mater* 2009;57:1367.
- [36] Hassan HA, Kecskes L, Lewandowski JJ. *Metall Mater Trans A* 2008;39:2077.
- [37] Gu XJ, McDermott AG, Poon SJ, Shiflet GJ. *Appl Phys Lett* 2006;88:211905.
- [38] Zhang ZF, Eckert J, Schultz L. *Acta Mater* 2003;51:1167.
- [39] Flores KM, Dauskardt RH. *J Mech Phys Solids* 2006;54:2418.
- [40] Yu P, Bai HY. *Mater Sci Eng A* 2008;485:1.
- [41] Gu XJ, Poon SJ, Shiflet GJ, Lewandowski JJ. *Scripta Mater* 2009;60:1027.
- [42] Johnson HH. *Mater Res Stand* 1965;5:442.
- [43] Xi XK, Zhao DQ, Pan MX, Wang WH, Wu Y, Lewandowski JJ. *Phys Rev Lett* 2005;94:125510.
- [44] Khonik SV, Granato AV, Joncich DM, Pompe A, Khonik VA. *Phys Rev Lett* 2008;100:065501.

- [45] Pan D, Inoue A, Sakurai T, Chen MW. *Proc Natl Acad Sci USA* 2008;105:14769.
- [46] Caris J, Lewandowski JJ. *Acta Mater* 2009. doi:10.1016/j.actamat.2009.10.018.
- [47] Lewandowski JJ, Lowhaphandu P. *Philos Mag A* 2002;82:3427.
- [48] Zhang Y, Zhao DQ, Wei BC, Wen P, Pan MX, Wang WH. *J Mater Res* 2001;16:1675.
- [49] Duan G, De Blauwe K, Lind ML, Schramm JP, Johnson WL. *Scripta Mater* 2008;58:159.
- [50] Wang WH. Institute of Physics, Chinese Academy of Sciences, Beijing, China, 2009, Private communication.
- [51] Lowhaphandu P, Lewandowski JJ. *Scripta Mater* 1998;38:1811.
- [52] Kimura H, Masumoto T. *Acta Metall* 1980;28:1663.
- [53] Flores KM, Dauskardt RH. *Scripta Mater* 1999;41:937.
- [54] Varadarajan R, Thurston AK, Lewandowski JJ. *Metall Mater Trans A* 2009. doi:10.1007/s11661-009-0059-z.
- [55] Deibler LA, Lewandowski JJ. *Mater Sci Eng A* 2009. doi:10.1016/j.msea.2009.10.072.
- [56] Gu XJ, Poon SJ, Shiflet GJ, Lewandowski JJ. Unpublished research, in preparation, 2009.
- [57] Nouri AS, Gu XJ, Poon SJ, Shiflet GJ, Lewandowski JJ. *Philos Mag Lett* 2008;88:853.